Inverse Problems **26** (2010) 115010 (21pp) doi:10.1088/0266-5611/26/11/115010

Finite-element contrast source inversion method for microwave imaging

Amer Zakaria[1], **Colin Gilmore**[2] **and Joe LoVetri**[1]

[1] Department of Electrical and Computer Engineering, University of Manitoba, Winnipeg, MB R3T 5V6, Canada
[2] Medical Physics, CancerCare Manitoba, Winnipeg, MB R3E 0V9, Canada

E-mail: azakaria@ee.umanitoba.ca, colin.gilmore@cancercare.mb.ca and Joe_LoVetri@umanitoba.ca

Received 17 May 2010, in final form 2 September 2010
Published 30 September 2010
Online at stacks.iop.org/IP/26/115010

Abstract

With respect to the microwave imaging of the dielectric properties in an imaging region, the full derivation of a new inversion algorithm based on the contrast source inversion (CSI) algorithm and a finite-element method (FEM) discretization of the Helmholtz differential operator formulation for the scattered electromagnetic field is presented. The unknown dielectric properties are represented as nodal values on a two-dimensional (2D) arbitrary triangular mesh using linear basis functions. The use of FEM to represent the Helmholtz operator allows for the flexibility of having an inhomogeneous background medium, as well as the ability to accurately model any boundary shape or type: both conducting and absorbing. The resulting sparse and symmetric FEM matrix equation can be solved efficiently, and it is shown how its solution can be used to calculate the gradient operators required in the conjugate-gradient CSI update without storing the inverse of the FEM matrix. The inversion algorithm is applied to conductive-enclosures of various shapes and unbounded-region microwave tomography configurations where the 2D transverse magnetic (TM) approximation can be applied.

(Some figures in this article are in colour only in the electronic version)

1. Introduction

Microwave imaging (MWI) is of interest for various applications such as geophysical surveying and medical imaging [1–3]. In the form of MWI considered herein, one attempts to quantitatively reconstruct the, mostly unknown, electrical properties (i.e. permittivity and/or conductivity) of an object of interest (OI) which is immersed in a background medium of known electrical properties. The OI is illuminated by various sources of microwave radiation

and the resulting field is measured at several locations within accessible regions surrounding the OI. The field produced by the same sources identically located within the background medium but in the absence of the OI, referred to as the incident field, is approximated through direct measurement and theoretical modeling. This general inverse scattering problem can be cast as an optimization problem over variables representing the unknown electrical properties which are to be reconstructed. The nonlinearity and ill-posedness of the problem can be treated by utilizing various optimization and regularization techniques [4–9].

The spatial domain for the mathematical problem can be assumed to be of infinite or finite extent with appropriate boundary conditions being imposed to approximate the physical demands of the experimental setup being considered. For example, in experimental setups used for biomedical imaging (BMI) applications where a lossy matching fluid is used, it is typical to assume a mathematical formulation which incorporates a spatial region of infinite extent and to impose appropriate radiative boundary conditions at infinity. Experimental setups using arbitrarily shaped conductive enclosures have also been investigated where the appropriate mathematical formulation assumes regions of finite extent with perfect electric conductor (PEC) boundary conditions being imposed on the appropriately shaped boundary [10–13]. In either case, the background medium can be assumed to be homogeneous or inhomogeneous.

When the inverse scattering problem formulation makes use of an integral equation (IE) for the electromagnetic field a Green's function corresponding to the background medium and the problem's boundaries is required. If the background medium is inhomogeneous or if the problem's boundary is complicated (e.g. arbitrary and/or conducting) deriving and calculating the Green's function can be a complex, computationally expensive process. With the knowledge of the Green's function, the IE is typically solved using the method-of-moments (MoM), which produces a dense system of equations that can be a computational burden [10, 14, 15].

Partial differential equation (PDE) formulations can be discretized directly using numerical techniques such as finite-difference (FD) or finite-element (FE) methods [16–18]. Using PDE operators, there is no need to determine the problem's Green function and, thus, the presence of an inhomogeneous background or a complicated boundary can be easily taken into account without affecting the computational complexity of the numerical solution. In addition, unlike IE formulations, PDE formulations readily produce sparse systems of equations which can be solved efficiently.

Most inversion algorithms are iterative techniques where estimates of the OI's electrical properties are updated starting from some initial guess. Some of such inversion algorithms require that a forward solver be called several times at each iteration to calculate the scattered fields associated with each transmitter for the current estimate of the OI's electrical properties; this can be a computational burden because the system of equations used to compute these scattered fields (whether using an IE or PDE formulation) must be assembled at each iteration. Examples of such algorithms are the distorted Born iteration method (DBIM), the Gauss–Newton inversion (GNI) and conjugate gradient using FEM [14–16]. A state-of-the art algorithm that has had much success in solving inverse scattering problems without the need to call a forward solver is the contrast source inversion (CSI) technique [19]. In each iteration of CSI, two variables—the contrast source and the contrast—are updated successively using a conjugate gradient method. The variables are updated to minimize a given cost functional. To enhance the quality of the reconstructions, and to increase its robustness to noisy data, regularization is introduced to the cost functional in the form of a weighted L_2-norm multiplicative constraint [20, 21]. The resulting method is called the multiplicative regularized

CSI (MR-CSI) method. The method has been applied successfully using the IE formulation in several applications [10, 22, 23].

The IE-CSI and IE-MRCSI methods are efficient if the Green's function is available analytically and is such as to produce integral equation operators which can be efficiently discretized and evaluated. This is indeed the case if the background medium is homogeneous and if the boundary is such as to allow a closed-form Green's function with the convolutional property (e.g. unbounded problem domains). To overcome these deficiencies in IE formulations, recently a finite-difference CSI (FD-CSI) method has been introduced in conjunction with a PDE formulation for the electromagnetic field [17, 24]. The FD-CSI algorithm uses an effective uniform structured grid discretization of the Helmholtz PDE and is thus a frequency-domain method. Using this technique one can incorporate an inhomogeneous background medium as well as various boundaries as long as these can be well approximated using the FD grid. Since the resulting FD matrix operator is independent of the OI, it does not change throughout the inversion process and the LU decomposition of its inverse can be calculated once and stored. The FD-CSI and its regularized counterpart FD-MRCSI have been used, successfully, for through-wall imaging, geophysical surveying and biomedical applications.

Despite its success, there are two major drawbacks inherent in FD-CSI. First, FD discretizations make it difficult to accurately model arbitrarily shaped boundaries, whether of the enclosure or of the unknown object, because of the use of structured rectangular grids requiring stair-stepping at curved boundaries. Although resolving the boundary is not an issue for unbounded-region configurations where absorbing boundary conditions are applied, it does become an issue for imaging configurations with conductive enclosures of arbitrary shape. Second, the use of structured rectangular grids becomes problematic when including prior information about the target because this usually requires the specification of electrical parameters on irregularly shaped regions [12, 24]. FEM discretizations of the governing PDE that use unstructured nonuniform meshes easily overcome these drawbacks as well as allowing the possibility of increasing the resolution of the reconstruction where it is needed in an adaptive way. That is, a higher density mesh can be imposed, either adaptively or initially if prior information is available, in regions where the spatial distribution of the electrical parameters varies highly. Adapting the mesh locally in regions of such high variation can increase the quality of the reconstruction while keeping the computational complexity of the inversion problem minimal.

In this paper, with the goal of capitalizing on these advantages of FEM discretizations, a novel inversion algorithm based on FEM combined with the contrast source inversion is presented. Preliminary results on this new algorithm were presented in [25], but full derivation of the algorithm with extensive testing were not. The algorithm is applied to two-dimensional (2D) transverse magnetic (TM) problems, but the method is extendable to 2D transverse electric problems and full three-dimensional (3D) vector formulations. The spatial domain is meshed using unstructured nonuniform triangular elements, with the electromagnetic field variables, as well as the electrical properties, specified at the nodes of the triangles and represented via the basis functions. The boundary of the problem can have any arbitrary shape and can be of any type. Similarly, the background medium can be taken to be inhomogeneous and is easily represented on such meshes. To demonstrate the advantages of this algorithm, it is used to invert synthetically generated datasets, as well as experimental data obtained using our own MWI prototype [26].

Inversion algorithms based on the finite-element method (FEM) have been introduced in the past. In [16], Rekanos *et al* use FEM for the field solution but the unknown electrical properties for the problem are located on a uniform grid of square cells. Each cell in the grid is

discretized into several triangles for the field solution. Such a dual-grid technique does not take advantage of the full flexibility of using an FEM discretization: the inversion is not actually performed on an arbitrary mesh. Furthermore, the method in [16] is only applied to synthetic datasets for unbounded-region problems and so the advantages of the FEM formulation for conductive enclosure setups are not investigated. In [18], Paulsen *et al* use a hybrid method that combines FEM and a boundary-element method (BEM). A dual mesh scheme is also used in their work, where the contrast variables are located on nodes of a coarse triangular mesh and the electric fields are calculated on a finer triangular mesh. At each iteration, the contrast variables are updated using a Gauss–Newton method and then the updates are utilized to calculate the scattered fields. This method has been applied successfully to experimental data [27]. A disadvantage of both of these FEM-based inversion algorithms is that the system of FEM equations has to be re-assembled at every iteration in order to solve for the scattered field. This disadvantage is not applicable to the this method wherein FEM is coupled with CSI.

2. Problem formulation

We consider the 2D TM problem with z-polarized electric field and an $\exp(j\omega t)$ time dependence[3]. The unknown isotropic OI is located within a bounded imaging domain $\mathcal{D}$, and the electric properties of the background medium, which can be inhomogeneous, are known. The permeability of the OI and background are taken to be that of free-space, μ_0. The enclosing boundary for the problem, Γ, can be of any shape, size or type depending on the imaging setup being modeled. The complex relative permittivity of the OI is denoted by $\epsilon_r(\boldsymbol{r})$, where $\boldsymbol{r} = (x, y)$ is the 2D position vector. The corresponding electric contrast is defined as

$$\chi(\boldsymbol{r}) = \frac{\epsilon_r(\boldsymbol{r}) - \epsilon_b(\boldsymbol{r})}{\epsilon_b(\boldsymbol{r})}, \tag{1}$$

where $\epsilon_b(\boldsymbol{r})$ is the complex relative permittivity of the background ($\chi(\boldsymbol{r}) = 0$ for $\boldsymbol{r} \notin \mathcal{D}$).

The imaging domain $\mathcal{D}$ is successively illuminated by one of T transmitters. The transmitters are assumed to be 2D point sources with the incident field, E_t^{inc}, produced by transmitter t, modeled by the scalar Helmholtz equation

$$\nabla^2 E_t^{\text{inc}}(\boldsymbol{r}) + k_b^2(\boldsymbol{r}) E_t^{\text{inc}}(\boldsymbol{r}) = j\omega\mu_0 J_t(\boldsymbol{r}), \tag{2}$$

where $\omega = 2\pi f$ is the angular frequency, and $k_b(\boldsymbol{r}) = \omega\sqrt{\mu_0\epsilon_0\epsilon_b(\boldsymbol{r})}$ is the background wavenumber which is allowed to be inhomogeneous. The source term, corresponding to transmitter t located at position $\boldsymbol{r}_t$, is given by

$$J_t(\boldsymbol{r}) = \frac{-1}{j\omega\mu_0}\delta(\boldsymbol{r} - \boldsymbol{r}_t). \tag{3}$$

With the OI present in the imaging domain, $\mathcal{D}$, the total field, E_t, satisfies the scalar Helmholtz equation

$$\nabla^2 E_t(\boldsymbol{r}) + k^2(\boldsymbol{r}) E_t(\boldsymbol{r}) = j\omega\mu_0 J_t(\boldsymbol{r}), \tag{4}$$

where $k(\boldsymbol{r}) = \omega\sqrt{\mu_0\epsilon_0\epsilon_r(\boldsymbol{r})}$. Thus, the Helmholtz equation satisfied by the scattered field, defined as $E_t^{\text{sct}}(\boldsymbol{r}) \triangleq E_t(\boldsymbol{r}) - E_t^{\text{inc}}(\boldsymbol{r})$, can be written as

$$\nabla^2 E_t^{\text{sct}}(\boldsymbol{r}) + k_b^2(\boldsymbol{r}) E_t^{\text{sct}}(\boldsymbol{r}) = -k_b^2(\boldsymbol{r}) w_t(\boldsymbol{r}), \tag{5}$$

where the contrast-source variables $w_t(\boldsymbol{r}) \triangleq \chi(\boldsymbol{r}) E_t(\boldsymbol{r})$ represent source terms which themselves depend on the total field.

[3] Note that with this assumption a time variable is no longer needed and that the index 't' will be used in the remainder of the paper to indicate the number corresponding to the active transmitter.

Solving for the incident field E_t^{inc} and the scattered field E_t^{sct} requires that boundary conditions (BCs) on Γ be defined. For a conductive-enclosure system perfect electrical conductor (PEC) boundary conditions are used resulting in homogeneous Dirichlet BCs, i.e.

$$E^{\text{inc}}(\boldsymbol{r} \in \Gamma) = 0 \qquad \text{and} \qquad E^{\text{sct}}(\boldsymbol{r} \in \Gamma) = 0. \tag{6}$$

For enclosed MWI systems incorporating sufficient loss in the matching medium such that little energy is reflected back from the boundaries of the enclosure, or for other imaging applications where such reflections can be ignored, a homogeneous lossy medium which extends to infinity can be assumed for the mathematical problem. In such cases all fields will be required to satisfy the 2D Sommerfeld radiation condition:

$$\lim_{r\to\infty} \sqrt{r}\left(\frac{\partial}{\partial r} E_t(\boldsymbol{r}) + jk_b E_t(\boldsymbol{r})\right) = 0, \tag{7}$$

where $r = \sqrt{x^2 + y^2}$. These boundary conditions are approximated at the FEM mesh boundary Γ using numerical radiation boundary conditions (RBCs) as summarized below.

3. Finite element method discretization

The problem domain (Ω) is discretized into a mesh of first-order triangular elements defined by N nodes. At each node, a linear basis function is specified, the parameters of which depend solely on the geometry of the mesh. We use the standard Rayleigh–Ritz formulation of FEM to discretize (5) which, irrespective of the type of BCs used, produces a matrix equation of the form [28]

$$[\mathbf{S} - \mathbf{T}_b]E_{t,\Omega}^{\text{sct}} = \mathbf{T}_b w_{t,\Omega}. \tag{8}$$

Here $\mathbf{S} \in \mathbb{C}^{N\times N}$ is the stiffness matrix, which depends on the BCs, and $\mathbf{T}_b \in \mathbb{C}^{N\times N}$ is the mass matrix, which depends on the background medium properties. The vectors $E_{t,\Omega}^{\text{sct}} \in \mathbb{C}^N$ and $w_{t,\Omega} \in \mathbb{C}^N$ contain the nodal values of the scattered field and the contrast source for transmitter t.

Entries in the ith row and jth column of the stiffness matrix (not arising from the boundary-integral term) and the mass matrix are given by

$$S_{i,j} = \int_\Omega \nabla\lambda_i \cdot \nabla\lambda_j \,\mathrm{d}s \qquad \text{and} \qquad T_{b_{i,j}} = \sum_{p=1}^{N} \int_\Omega k_{b,p}^2 \lambda_i \lambda_j \lambda_p \,\mathrm{d}s, \tag{9}$$

where λ_i, λ_j and λ_p are the linear basis functions defined at the ith, jth and pth node, respectively, ∇ is a spatial gradient operator and $k_{b,p}$ is the background wavenumber at node p.

The Sommerfeld radiation BCs are modeled using second-order absorbing BCs [28]:

$$\nabla E_t^{\text{sct}}(\boldsymbol{r}) \cdot \hat{n} + \gamma_1(\boldsymbol{r}) E_t^{\text{sct}}(\boldsymbol{r}) = -\gamma_2(\boldsymbol{r}) \frac{\partial^2 E_t^{\text{sct}}(\boldsymbol{r})}{\partial \xi^2} \qquad \text{for} \quad \boldsymbol{r} \in \Gamma, \tag{10}$$

where $\hat{n}$ denotes the outward-normal unit vector, ξ is the arc length measured along the boundary,

$$\gamma_1(\boldsymbol{r}) = jk_b(\boldsymbol{r}) + \frac{\kappa(\xi)}{2} - \frac{\kappa^2(\xi)}{8(j\kappa(\xi) - k_b(\boldsymbol{r}))}, \qquad \gamma_2(\boldsymbol{r}) = -\frac{j}{2(j\kappa(\xi) - k_b(\boldsymbol{r}))} \tag{11}$$

and $\kappa(\xi)$ is the curvature of the boundary at ξ [28, p 128]. The FEM formulation of the BCs leads to a boundary integral term that contributes to the (i,j)th element of $\mathbf{S}$ as

$$S_{i,j}^{\Gamma} = \int_\Gamma \left(\gamma_1 \lambda_i^\Gamma \lambda_j^\Gamma - \gamma_2 \frac{\partial \lambda_i^\Gamma}{\partial \xi} \frac{\partial \lambda_j^\Gamma}{\partial \xi}\right) \mathrm{d}l. \tag{12}$$

Here λ_i^Γ, λ_j^Γ are linear boundary basis functions defined for nodes i and j on Γ.

3.1. Matrix operators

The FEM-CSI algorithm we present here was inspired by the FD-CSI formulation presented in [17]. Clearly, any discretization of the PDE formulation of the problem can be used in conjunction with the CSI algorithm. The FEM-CSI algorithm can be described more effectively by introducing several matrix operators.

The first operator $\boldsymbol{\mathcal{M}}_{\mathcal{S}} \in \mathbb{C}^{R\times N}$ transforms field values from the N problem domain nodes to the R receiver locations on the measurement surface $\mathcal{S}$; if the receiver locations are within the problem's mesh the operator interpolates to these locations using the FEM basis functions, while if the receivers are located outside the mesh (for example, in unbounded-region problems the receivers may be located in the far-field region), Huygens' principle is used to find the field at the receiver locations [28]. The second operator $\boldsymbol{\mathcal{M}}_{\mathcal{D}} \in \mathbb{R}^{I\times N}$ simply *selects* the field values at the I nodes within the imaging domain $\mathcal{D}$. Both matrices operate on vectors containing values at all mesh nodes.

At each iteration of the inversion algorithm, the contrast source variables $w_t \in \mathbb{C}^I$ are available at nodes within $\mathcal{D}$; however, the FEM matrix equation requires the contrast source variables at all mesh nodes. The contrast source variables $w_{t,\Omega} \in \mathbb{C}^N$, for all nodes in Ω, are given by

$$w_{t,\Omega} = \boldsymbol{\mathcal{M}}_{\mathcal{D}}^T w_t, \tag{13}$$

where the superscript T denotes the transpose. Substituting (13) into the FEM matrix equation, a new operator $\boldsymbol{\mathcal{L}} \in \mathbb{C}^{N\times I}$ is defined as

$$E_{t,\Omega}^{\text{sct}} = \boldsymbol{\mathcal{L}}[w_t] = (\mathbf{S} - \mathbf{T}_b)^{-1}\mathbf{T}_b \boldsymbol{\mathcal{M}}_{\mathcal{D}}^T[w_t]. \tag{14}$$

3.2. Solving the linear matrix equation

An efficient LU decomposition algorithm can be utilized for calculating the inverse in the operator $\boldsymbol{\mathcal{L}}$, as matrices $\mathbf{S}$ and $\mathbf{T}_b$ are sparse and symmetric. Here the Unsymmetric-Pattern Multifrontal Package (UMFPACK) with column pre-ordering, which is available in MATLAB, is used [29, 30]. For a given problem, the LU decomposition is performed once and the resulting matrices are saved and recalled when necessary. Then, for solving the linear matrix equation, efficient matrix factorization algorithms included with UMFPACK are used.

Another direct solver package that can be used for sparse matrix LU decomposition and factorization is PARDISO (parallel sparse direct linear solver). Although it is a direct solver, PARDISO supports a combination of direct and iterative methods to accelerate the linear solution process [31]. PARDISO often uses less memory than UMFPACK; however, it is not used or tested in this paper.

A disadvantage of using sparse LU decomposition algorithms is that it requires more memory, especially for 3D problems, making their use inefficient. An alternative would be using iterative solvers like GMRES (generalized minimal residual method) and CG (conjugate gradient). Although they are more memory-efficient, iterative solvers might be less stable and have slow convergence; therefore, appropriate preconditioning techniques have to be tested and used.

3.3. Norms and inner products

With the unknown variables located at the nodes of the the triangular mesh, the L_2-norm and the inner product in $\mathcal{D}$ are calculated as

$$\|x\|_{\mathcal{D}}^2 = x^H \mathbf{T}_{\mathcal{D}} x \qquad \text{and} \qquad \langle x, y\rangle_{\mathcal{D}} = y^H \mathbf{T}_{\mathcal{D}} x, \tag{15}$$

where x and y are arbitrary vectors of size I, the superscript H denotes the Hermitian (complex conjugate transpose) and $\mathbf{T}_{\mathcal{D}} \in \mathbb{R}^{I\times I}$ is the mass matrix restricted to nodes lying within the imaging domain $\mathcal{D}$. The (i,j)th element of $\mathbf{T}_{\mathcal{D}}$ is given by

$$T_{\mathcal{D}_{i,j}} = \int_{\mathcal{D}} \lambda_i \lambda_j \, \mathrm{d}s. \tag{16}$$

Assuming that the receiver locations on the surface $\mathcal{S}$ are distributed uniformly, the L_2-norm and the inner product on $\mathcal{S}$ are given as

$$\|x\|_{\mathcal{S}}^2 = x^H x \qquad \text{and} \qquad \langle x, y\rangle_{\mathcal{S}} = y^H x, \tag{17}$$

where x and y are vectors of size R.

4. The inversion algorithm

In the framework of the contrast source inversion (CSI) [19], the objective is to update the contrast source and the contrast variables sequentially, so as to minimize the following cost functional:

$$\begin{aligned}\mathcal{F}(\chi, w_t) &= \mathcal{F}^{\mathcal{S}}(w_t) + \mathcal{F}^{\mathcal{D}}(\chi, w_t)\\ &= \frac{\sum_t \|f_t - \boldsymbol{\mathcal{M}}_{\mathcal{S}}\boldsymbol{\mathcal{L}}[w_t]\|_{\mathcal{S}}^2}{\sum_t \|f_t\|_{\mathcal{S}}^2} + \frac{\sum_t \|\chi \odot E_t^{\mathrm{inc}} - w_t + \chi \odot \boldsymbol{\mathcal{M}}_{\mathcal{D}}\boldsymbol{\mathcal{L}}[w_t]\|_{\mathcal{D}}^2}{\sum_t \|\chi \odot E_t^{\mathrm{inc}}\|_{\mathcal{D}}^2}.\end{aligned} \tag{18}$$

Here, $f_t \in \mathbb{C}^R$ holds the measured scattered field data at the R receiver locations for each transmitter, $\chi \in \mathbb{C}^I$ is the vector of contrast nodal values for nodes located inside $\mathcal{D}$, and $E_t^{\mathrm{inc}} = \boldsymbol{\mathcal{M}}_{\mathcal{D}}\big[E_{t,\Omega}^{\mathrm{inc}}\big]$ is the vector of the incident field corresponding to transmitter t for nodes inside $\mathcal{D}$. The notation $a \odot b$ denotes the Hadamard (i.e. element-wise) product.

In CSI, the first step is to update contrast source variables w_t by a conjugate-gradient (CG) method with Polak–Ribière search directions, while assuming the contrast variables χ constant. In the second step, w_t is assumed constant, and a modified form of the domain equation ($\mathcal{F}^{\mathcal{D}}(\chi, w_t)$) is minimized (this second step has a closed-form solution) [19]. The first update equation in the CSI method is

$$w_{t,n} = w_{t,n-1} + \alpha_{t,n} d_{t,n}, \tag{19}$$

where the subscript n is the iteration number, $\alpha_{t,n}$ is the update step-size and $d_{t,n}$ are Polak–Ribière search directions. The step-size $\alpha_{t,n}$ is determined as

$$\alpha_{t,n} = \arg\min_{\alpha}\{\mathcal{F}(w_{t,n-1} + \alpha d_{t,n}, \chi_{n-1})\}, \tag{20}$$

for which a closed-form expression can be found by introducing $w_{t,n-1} + \alpha d_{t,n}, \chi_{n-1}$ in (18) and setting the derivative with respect to α equal to zero. The result is

$$\alpha_{t,n} = \frac{\eta^{\mathcal{S}}\langle \rho_{t,n-1}, \boldsymbol{\mathcal{M}}_{\mathcal{S}}\boldsymbol{\mathcal{L}}[d_{t,n}]\rangle_{\mathcal{S}} + \eta_n^{\mathcal{D}}\langle r_{t,n-1}, d_{n,t} - \chi_{n-1} \odot \boldsymbol{\mathcal{M}}_{\mathcal{D}}\boldsymbol{\mathcal{L}}[d_{t,n}]\rangle_{\mathcal{D}}}{\eta^{\mathcal{S}}\|\boldsymbol{\mathcal{M}}_{\mathcal{S}}\boldsymbol{\mathcal{L}}[d_{t,n}]\|_{\mathcal{S}}^2 + \eta_n^{\mathcal{D}}\|d_{n,t} - \chi_{n-1} \odot \boldsymbol{\mathcal{M}}_{\mathcal{D}}\boldsymbol{\mathcal{L}}[d_{t,n}]\|_{\mathcal{D}}^2}. \tag{21}$$

Here the normalization factors $\eta^{\mathcal{S}}$ and $\eta_n^{\mathcal{D}}$ are

$$\begin{aligned}\eta^{\mathcal{S}} &= \left(\sum_t \|f_t\|_{\mathcal{S}}^2\right)^{-1},\\ \eta_n^{\mathcal{D}} &= \left(\sum_t \|\chi_{n-1} \odot E_t^{\mathrm{inc}}\|_{\mathcal{D}}^2\right)^{-1},\end{aligned} \tag{22}$$

and the error terms $\rho_{t,n-1}$ and $r_{t,n-1}$ are

$$\begin{aligned}\rho_{t,n-1} &= f_t - \boldsymbol{\mathcal{M}}_{\mathcal{S}}\boldsymbol{\mathcal{L}}[w_{t,n-1}],\\ r_{t,n-1} &= \chi_{n-1} \odot E_t^{\text{inc}} - w_{t,n-1} + \chi_{n-1} \odot \boldsymbol{\mathcal{M}}_{\mathcal{D}}\boldsymbol{\mathcal{L}}[w_{t,n-1}].\end{aligned} \tag{23}$$

The Polak–Ribière search directions $d_{t,n}$ are calculated by the following formula:

$$d_{t,n} = -g_{t,n} + \frac{\langle g_{t,n}, g_{t,n} - g_{t,n-1}\rangle_{\mathcal{D}}}{\|g_{t,n-1}\|_{\mathcal{D}}^2} d_{t,n-1}, \tag{24}$$

where $g_{t,n}$ is the gradient of the cost function $\mathcal{F}(\chi, w_t)$ with respect to the contrast sources $w_{t,n}$.

Using an approach similar to [17], the gradient $g_{t,n}$ is given by

$$g_{t,n} = -2\eta^{\mathcal{S}}\mathbf{T}_{\mathcal{D}}{}^{-1}\boldsymbol{\mathcal{L}}^H\boldsymbol{\mathcal{M}}_{\mathcal{S}}^H\rho_{t,n-1} - 2\eta_n^{\mathcal{D}}\mathbf{T}_{\mathcal{D}}^{-1}\big(\mathbf{I} - \boldsymbol{\mathcal{L}}^H\boldsymbol{\mathcal{M}}_{\mathcal{D}}^T\mathbf{X}_{n-1}^H\big)\mathbf{T}_{\mathcal{D}}r_{t,n-1} \tag{25}$$

where $\mathbf{I} \in \mathbb{R}^{I\times I}$ is an identity matrix and $\mathbf{X}_{n-1} = \text{diag}(\chi_{n-1})$ is a diagonal matrix. The derivation of this gradient expression is outlined in appendix A.

After updating the contrast source variables, χ is evaluated by minimizing the modified domain equation $\mathcal{F}_m^{\mathcal{D}}(\chi)$ given by

$$\mathcal{F}_m^{\mathcal{D}}(\chi) = \sum_t \big\|\chi \odot E_t^{\text{inc}} - w_t + \chi \odot \boldsymbol{\mathcal{M}}_{\mathcal{D}}\boldsymbol{\mathcal{L}}[w_t]\big\|_{\mathcal{D}}^2. \tag{26}$$

The contrast source variables w_t are assumed constant in this minimization. At the nth iteration, this requires the solution of the following sparse matrix equation for χ_n:

$$\left(\sum_t \mathbf{E}_{t,n}^H\mathbf{T}_{\mathcal{D}}\mathbf{E}_{t,n}\right)\chi_n = \sum_t \mathbf{E}_{t,n}^H\mathbf{T}_{\mathcal{D}}w_{t,n}. \tag{27}$$

Here, $\mathbf{E}_{t,n} \in \mathbb{C}^{I\times I}$ is the total field diagonal matrix; the diagonal entities are the elements of vector $E_{t,n} = E_t^{\text{inc}} + \boldsymbol{\mathcal{M}}_{\mathcal{D}}\boldsymbol{\mathcal{L}}[w_{t,n}]$. The derivation of the contrast update is given in appendix B.

4.1. Initializing FEM-CSI algorithm

The initial guess of the contrast source variables cannot be set to zero since the cost functional becomes undefined at the first iteration. As in the standard CSI algorithm [19], the initial guess for the FEM-CSI is evaluated by calculating the contrast source variables that will minimize the data misfit $\mathcal{F}^{\mathcal{S}}(w_t)$. This minimizer is taken to be the result of applying the method of steepest descent to $\mathcal{F}^{\mathcal{S}}(w_t)$. As outlined in appendix C, this initial guess can be given in the closed form as

$$w_{t,0} = \frac{\text{Re}\langle\boldsymbol{\mathcal{M}}_{\mathcal{S}}\boldsymbol{\mathcal{L}}[\boldsymbol{\mathcal{G}}^{\mathcal{S}}f_t], f_t\rangle_{\mathcal{S}}}{\|\boldsymbol{\mathcal{M}}_{\mathcal{S}}\boldsymbol{\mathcal{L}}[\boldsymbol{\mathcal{G}}^{\mathcal{S}}f_t]\|_{\mathcal{S}}^2}\boldsymbol{\mathcal{G}}^{\mathcal{S}}f_t, \tag{28}$$

where the operator $\boldsymbol{\mathcal{G}}^{\mathcal{S}} = -2\eta^{\mathcal{S}}\mathbf{T}_{\mathcal{D}}^{-1}\boldsymbol{\mathcal{L}}^H\boldsymbol{\mathcal{M}}_{\mathcal{S}}^H$. After evaluating $w_{t,0}$, the initial guess for the contrast variables χ is calculated using (27) and the initial Polak–Ribière search directions $d_{t,0}$ are set to zero.

5. Inversion results

In this section, a comparison between the inversion results from FEM-CSI and IE-CSI is performed first using the same synthetic dataset. Next, FEM-CSI is utilized to invert several synthetic datasets and one experimental dataset.

Synthetic dataset inversions are used to show two advantages of the FEM-CSI algorithm: the capability of incorporating an inhomogeneous background, and the ability to model non-circular PEC enclosures. All synthetic datasets are created using an FEM forward solver. The meshes used to generate the synthetic datasets in FEM are different from those used in the inversion algorithm to invert the scattered field data. All the geometries and meshes are generated using the third-party freeware GMSH [32]. To ensure accurate calculations of the electric field, the characteristic mesh length (CL) of different meshes is selected to be less than $\lambda/15$ where λ is the smallest expected wavelength for a given problem. For synthetic data examples, CL values of the forward mesh and inversion mesh are different. For all the synthetic measured scattered fields 3% noise is added as follows [34]:

$$f_t^{\text{noisy}} = f_t + \max\left(\forall_t \, |f_t|\right) \frac{\eta}{\sqrt{2}} (\tau_1 + j\tau_2), \tag{29}$$

where f_t is the measured scattered field on the domain $\mathcal{S}$ obtained from the forward solver, τ_1 and τ_2 are uniformly distributed random numbers between -1 and 1, and η is the desired fraction of the noise. For the synthetic datasets used herein, $\eta = 0.03$.

In the inversion for each dataset, the algorithm is allowed to run for 1024 iterations within which in all cases considered, the algorithm converged. In addition, the predicted contrast after each iteration is constrained to remain within physical bounds (i.e. the real part of the relative permittivity is kept greater than 1, and the conductivity is constrained to be a positive value).

To assess the quality of the synthetic data reconstructions, for each dataset the relative error (*Err*) between the exact OI profile and the reconstructed image is calculated. This error is defined as

$$Err = \frac{\|\epsilon_{\text{exact}}(\boldsymbol{r}) - \epsilon_{\text{reconst}}(\boldsymbol{r})\|_{\mathcal{D}}}{\|\epsilon_{\text{exact}}(\boldsymbol{r})\|_{\mathcal{D}}}. \tag{30}$$

Since the exact profile and the inversion results are located on different arbitrary triangular meshes, it is necessary to interpolate them to the same uniform square grid to calculate *Err*. This uniform grid is discretized to a finer and finer square cells until the calculated *Err* converges.

Finally, a summary of inversions is provided in table 2 where the frequency (f), the number of transmitters (T), the number of nodes in Ω (N), the number of nodes in $\mathcal{D}$ (I) and the average time per iteration ($\tilde{t}_{\text{iter}}$) are specified for each example. The inversion algorithm is implemented in MATLAB® and is running on a PC workstation with two Intel® Xeon® quad-core 2.8 GHz processors.

5.1. Comparison between FEM-CSI and IE-CSI

For comparing FEM-CSI and IE-CSI, we consider the U-umlaut (Ü) profile depicted in figures 1(a) and (d). In this profile, the OI consists of scatterers arranged in the 'Ü' shape having the same relative permittivity of $\epsilon_r = 2 - j1$. The OI is located in an unbounded homogeneous background medium with relative permittivity $\epsilon_b = 1$. The OI is illuminated by 16 transmitters at a frequency of $f = 2$ GHz and the data are collected using 16 receivers per transmitter. The transmitting and receiving points are evenly spaced on a circle of radius 0.225 m. In both FEM-CSI and IE-CSI, the inversion domain $\mathcal{D}$ is a square centered in the middle of the problem domain with side length equal to 0.15 m. In FEM-CSI, the inversion mesh consists of unstructured arbitrarily oriented triangles with 3139 nodes within $\mathcal{D}$. The IE-CSI inversion grid consists of 100×100 cells confined within the boundaries of $\mathcal{D}$.

The reconstruction results of FEM-CSI are shown in figures 1(b) and (e) and for IE-CSI in figures 1(c) and (f). Further, the progress of the cost functionals of FEM-CSI and IE-CSI

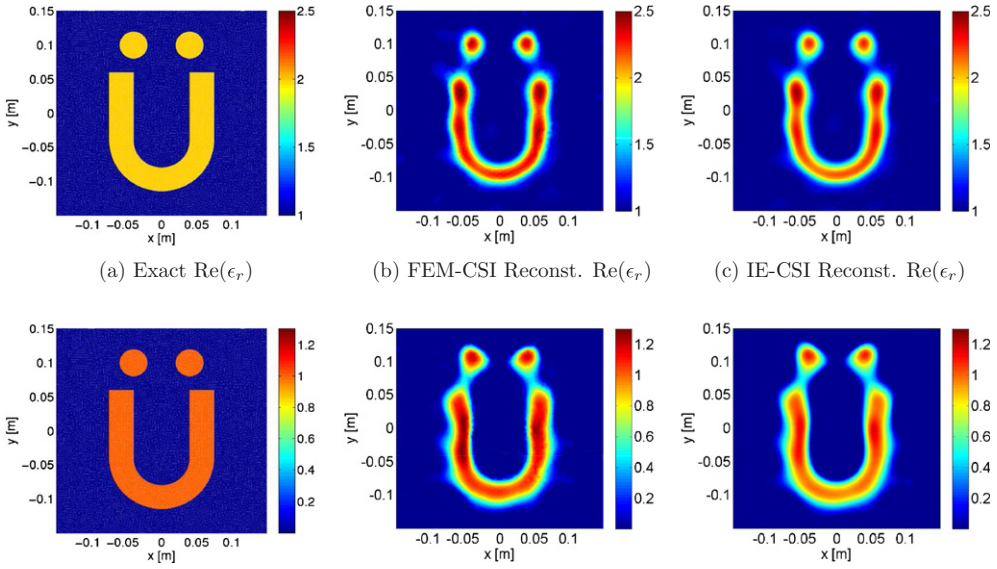

(a) Exact $\mathrm{Re}(\epsilon_r)$ (b) FEM-CSI Reconst. $\mathrm{Re}(\epsilon_r)$ (c) IE-CSI Reconst. $\mathrm{Re}(\epsilon_r)$

(d) Exact $-\mathrm{Im}(\epsilon_r)$ (e) FEM-CSI Reconst. $-\mathrm{Im}(\epsilon_r)$ (f) IE-CSI Reconst. $-\mathrm{Im}(\epsilon_r)$

Figure 1. Ü exact profile (a), (d) and reconstructions at $f = 2$ GHz using FEM-CSI (b), (e) and IE-CSI (c), (f).

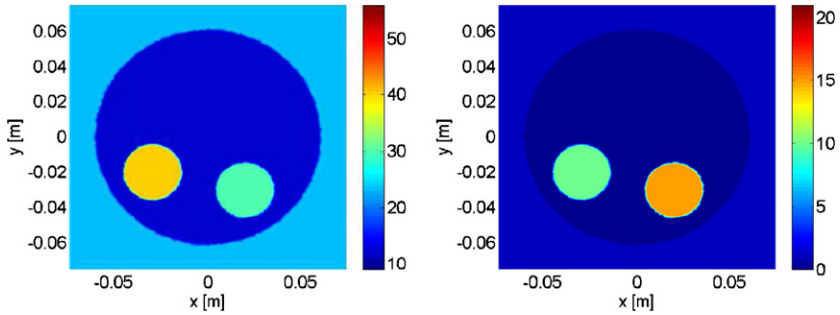

(a) Exact $\mathrm{Re}(\epsilon_r)$ (b) Exact $-\mathrm{Im}(\epsilon_r)$

Figure 2. Exact profile of circular targets with a lossy background at a frequency of $f = 1$ GHz.

are shown in figure 8(a). Comparing the reconstructions, the results of both FEM-CSI and IE-CSI are similar. For FEM-CSI $Err = 18.06\%$ while for IE-CSI $Err = 17.73\%$. Both algorithms were able to resolve the different features of the OI; however, both reconstructions of the real and imaginary relative permittivity values are higher than expected.

Differences between FEM-CSI and IE-CSI reconstructions arise because FEM-CSI is performed on an irregular mesh of arbitrary triangular elements while in IE-CSI the inversion domain is a regular uniform grid of square cells. These differences can be reduced by using a uniform mesh of equilateral triangles in FEM-CSI, applying a spatial filtering technique on FEM-CSI result at each iteration [33], or using multiplicative regularization. Furthermore, the

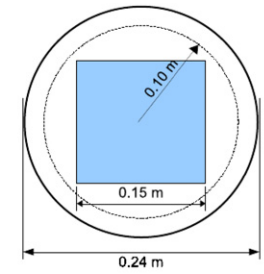

(a) Circular Enclosure

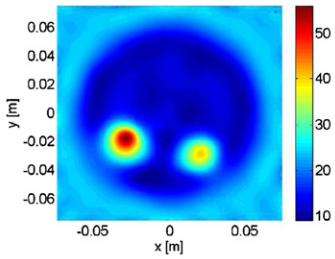

(b) Reconst. $\mathrm{Re}(\epsilon_r)$

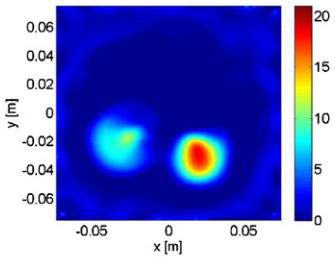

(c) Reconst. $-\mathrm{Im}(\epsilon_r)$

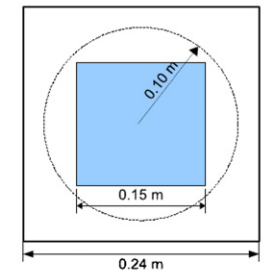

(d) Square Enclosure

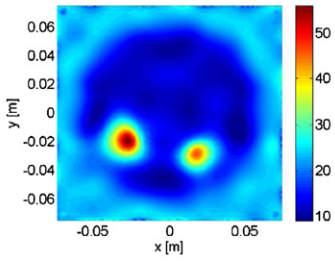

(e) Reconst. $\mathrm{Re}(\epsilon_r)$

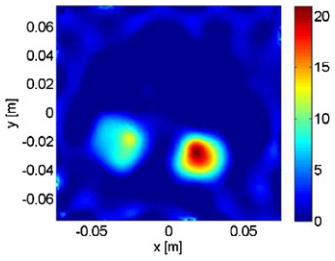

(f) Reconst. $-\mathrm{Im}(\epsilon_r)$

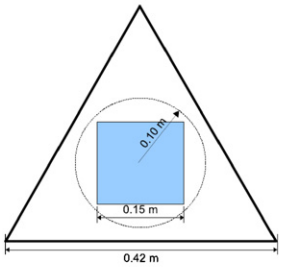

(g) Triangular Enclosure

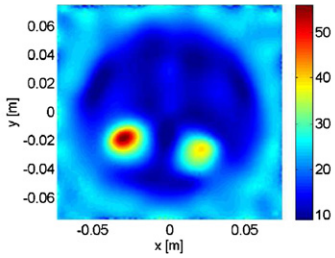

(h) Reconst. $\mathrm{Re}(\epsilon_r)$

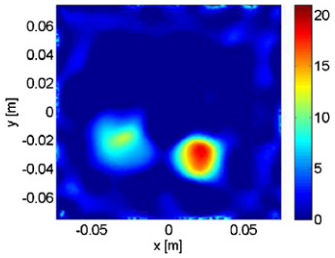

(i) Reconst. $-\mathrm{Im}(\epsilon_r)$

Figure 3. PEC enclosure configurations and FEM-CSI reconstructions at $f = 2$ GHz for a circular domain (a)–(c), square domain (d)–(f) and triangular domain (g)–(i).

cost functionals of FEM-CSI and IE-CSI converge to different values because the synthetic dataset is generated using FEM, the numerical noise floor of both algorithms is different (FEM-CSI implemented in MATLAB while IE-CSI in C++) and again the inversion domain properties are not the same.

5.2. Microwave tomography in PEC enclosures of various shapes

As previously mentioned, one advantage of FEM-CSI is the ability to perform imaging in different PEC enclosure shapes without any modification to the algorithm. The concept of imaging inside enclosures of arbitrary shapes was introduced before using a Gauss–Newton inversion (GNI) algorithm in [12]. To illustrate this feature, we consider an OI which consists

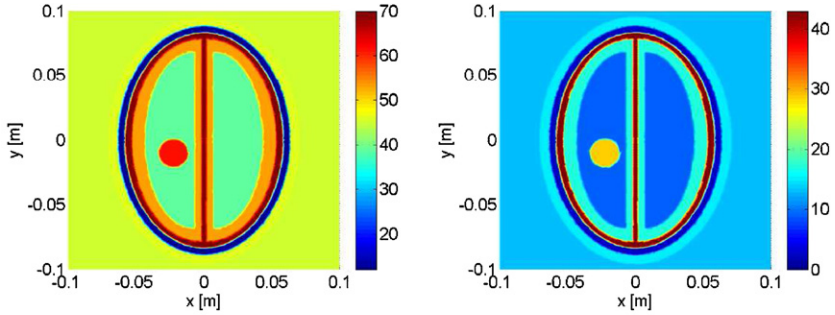

(a) Exact $\mathrm{Re}(\epsilon_r)$ (b) Exact $-\mathrm{Im}(\epsilon_r)$

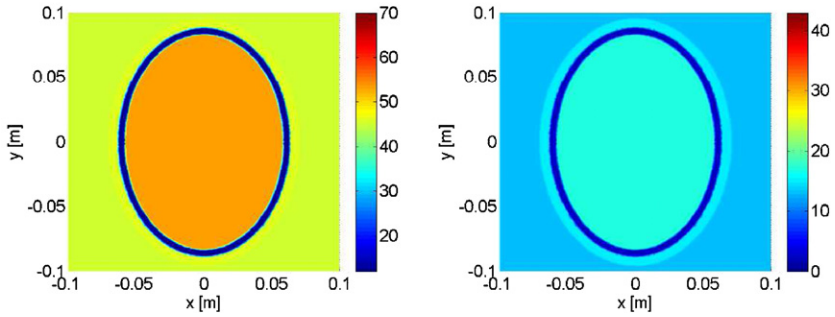

(c) prior $\mathrm{Re}(\epsilon_r)$ (d) prior $-\mathrm{Im}(\epsilon_r)$

Figure 4. Brain exact profile (a), (b) and given prior information (c), (d) at $f = 1$ GHz.

of three circular regions. One of the circular regions has a radius of 0.06 m with a relative permittivity of $\epsilon_r = 12$. In this region, the other two circular regions are embedded. The two regions have the same radius of 0.015 m with relative permittivities of $\epsilon_r = 40 - j10$ and $\epsilon_r = 30 - j15$ at a frequency of $f = 1$ GHz. This OI has been used in other publications such as [13, 25]. The target configuration is shown in figures 2(a) and (b).

The OI is centered within three different PEC enclosures of different shapes: a circle of radius 0.12 m, a square with side of 0.24 m and an equilateral triangle of side length equal to 0.42 m. The dimensions of each enclosure are depicted in figures 3(a), (d) and (g). In all enclosures, the OI is surrounded by a background medium of relative permittivity $\epsilon_b = 23.4 - j1.13$ at a frequency of $f = 1$ GHz. The OI is interrogated by 32 transmitters at a frequency of $f = 1$ GHz and the scattered data are collected at 32 receivers per transmitter. For all enclosures, the transmitting and receiving points are evenly spaced and located on a circle of radius 0.1 m.

The inversion domain $\mathcal{D}$ is a square centered in the middle of the enclosures with the square's side length equal to 0.15 m. The number of unknowns in $\mathcal{D}$ are approximately 6000 for all cases. For any enclosure, the unknowns are positioned on the vertices of triangles in an unstructured arbitrary mesh. The reconstructions after 1024 iterations are shown in figures 3(b) and (c) for circular enclosure, (e), (f) for square and (h), (i) for triangular, and the cost functional progress is given in figure 8(b). The relative errors in the reconstructions for the three different enclosures are relatively similar with $Err_{\text{circle}} = 18.25\%$, $Err_{\text{square}} = 19.22\%$

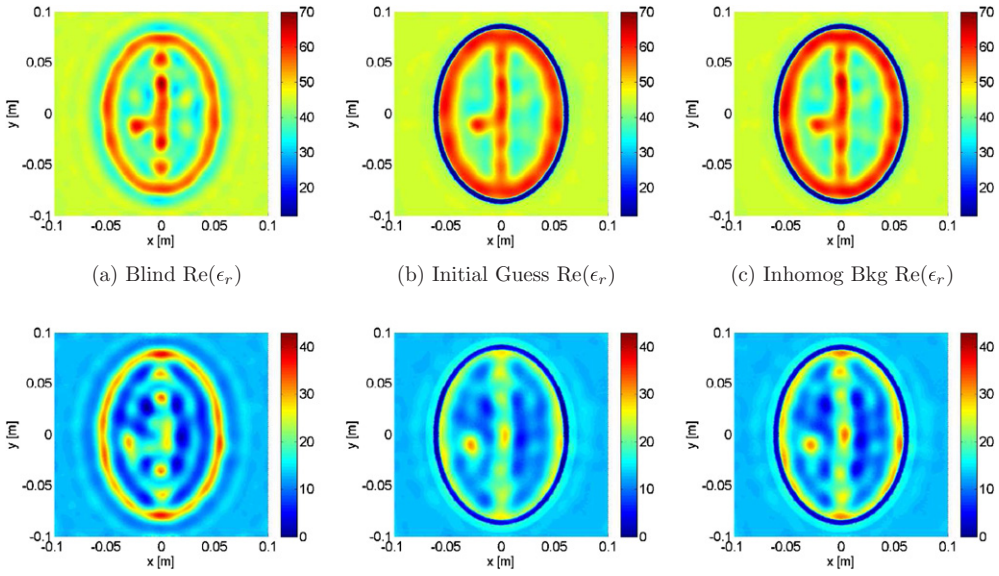

(a) Blind $\mathrm{Re}(\epsilon_r)$ (b) Initial Guess $\mathrm{Re}(\epsilon_r)$ (c) Inhomog Bkg $\mathrm{Re}(\epsilon_r)$

(d) Blind $-\mathrm{Im}(\epsilon_r)$ (e) Initial Guess $-\mathrm{Im}(\epsilon_r)$ (f) Inhomog Bkg $-\mathrm{Im}(\epsilon_r)$

Figure 5. FEM-CSI reconstructions at $f = 1$ GHz when no prior information is given (a), (d), when prior information is utilized as initial guess (b), (e), and when prior information is used as background (c), (f).

Table 1. Relative dielectric permittivities of the brain model at a frequency of $f = 1$ GHz.

Skin	Skull	CSF	GM	WM	Stroke
$46 - j15$	$12.8 - j2.4$	$69.3 - j42.8$	$52.8 - j16.9$	$38.6 - j9.0$	$61.1 - j28.5$

and $Err_{\text{triangular}} = 19.28\%$. The OI features are well resolved using any of the PEC enclosure shapes.

5.3. Biological imaging with an inhomogeneous background

To demonstrate the capability of FEM-CSI to employ prior information as the inhomogeneous background, the third OI is selected as a simplified model of a brain exhibiting symptoms of a stroke. This brain model is based on that published in [35] and similar such models have been used in [15, 24]. It consists of an outer skin region followed by the skull, the cerebral-spinal fluid (CSF), the gray matter (GM) and the white matter (WM). A stroke region representing a blood clot is located on the left side of the white matter region. The relative permittivities of the different biological regions in the model are summarized in table 1 for a frequency of $f = 1$ GHz. The permittivity values of the model are based on the result of a study reported in [36].

The brain model is located in a background medium of permittivity $\epsilon_b = 45 - j13$. The target is irradiated by 32 transmitters evenly spaced on a circle of radius 0.11 m at a frequency of $f = 1$ GHz. The data are collected at 32 receivers per transmitter where the receiver locations are the same as the transmitter locations. The inversion domain $\mathcal{D}$ is a square centered in the problem domain with its side lengths equal to 0.20 m. The number of

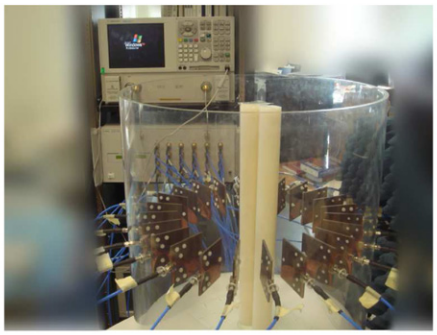

(a) Measurement Setup and MWI System

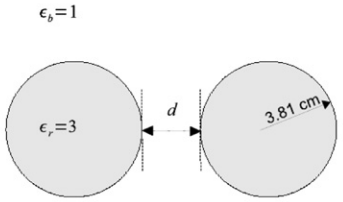

(b) Schematic of Scattering Cylinders

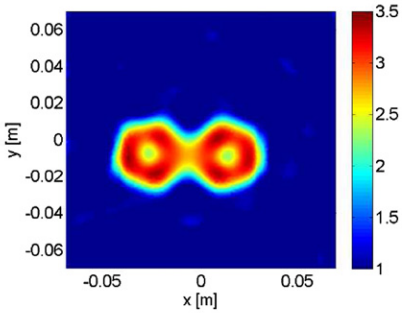

(c) Reconst. for $d = 0$ m

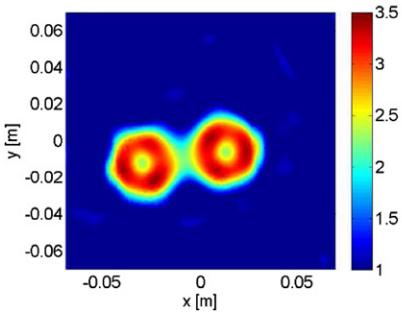

(d) Reconst. for $d = 0.005$ m

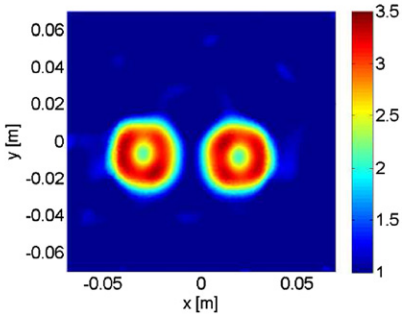

(e) Reconst. for $d = 0.01$ m

Figure 6. Reconstructions at $f = 4.5$ GHz for experimental datasets of two nylon-66 rods separated by 0 m (a), 0.005 m (b) and 0.01 m (c).

unknowns (located at the mesh nodes) within $\mathcal{D}$ is 12 131 nodes. The inversion algorithm is run three successive times. In the first run, blind inversion is performed with no prior information given to the algorithm. For the second simulation, the prior data depicted in figures 4(c) and (d) is given to the algorithm as an initial guess. The third simulation was executed using the prior information as an inhomogeneous background by incorporating this information within the $\mathcal{L}[\cdot]$ operator.

Table 2. Summary of FEM-CSI inversion examples.

Example	f (GHz)	T	N	I	$\tilde{t}_{\text{iter}}$ (s)
Ü-profile (figure 1)	2	16	13 539	3139	0.99
PEC enclosures (figure 3)	1	32			
Circular			12 352	6027	2.51
Square			15 584	5936	2.79
Triangular			20 382	5951	3.28
Brain model (figure 5)	1	32	21 689	12 131	5.96
Experimental (figure 6)	4.5	24	23 145	10 841	4.35

The reconstruction results after 1024 iterations are shown in figures 5(a) and (d) for blind inversion, (b), (e) when the prior information is used as an initial guess and (c), (f) when the prior information is used as the inhomogeneous background. The FEM-CSI cost functional progress for each case is given in figure 8(c). The features of the brain model with the stroke are resolved in all three cases; however, the best reconstruction is obtained with the prior information used as the inhomogeneous background (inhomog bkg). The relative errors for the different runs are $Err_{\text{blind}} = 22.49\%$, $Err_{\text{initial}} = 14.54\%$ and $Err_{\text{inhomog}} = 13.91\%$. The relative errors verify that using the prior information as an inhomogeneous background for the inversion produced the best results.

5.4. Inversion of experimental datasets

The experimental dataset was collected using our air-filled MWI system that has been reported in [26, 37, 38]. A picture of the system is given in figure 6(a). The system uses a two-port Agilent vector network analyzer (VNA) as a microwave source and receiver. The VNA is connected to the antennas via an Agilent 24-port microwave switch. The antennas utilized are 24 Vivaldi antennas arranged in a circular array of radius ≈ 0.22 m. For each transmitting antenna, 23 measurements are collected; thus, the total number of measurements per dataset is $23 \times 24 = 552$. The collected data are then calibrated using the procedure detailed in [26]. The experimental datasets are collected at a frequency of $f = 4.5$ GHz.

Two canonical nylon-66 cylinders are selected as targets. Each cylinder has a radius of 0.0381 m and a height of 0.44 m with a relative permittivity $\epsilon_r \approx 3$ at a frequency of $f = 4.5$ GHz. The two cylinders are centered in the middle of the system's chamber, with the separation between them varied to $d = 0$ m, $d = 0.005$ m and $d = 0.01$ m. The configuration of the two targets and the separation between them is shown in figure 6(b). For inverting the experimental datasets, the domain $\mathcal{D}$ is selected to be a square centered in the middle of the problem domain with its side length equal to 0.15 m. The number of nodes within the $\mathcal{D}$ is 10 841.

The reconstructions for the different separations are shown in figures 6(c)–(e), while the progress of the cost functional for each separation is given in figure 8(d). As the imaginary part of the surrounding medium (air) and the nylon-66 rods is negligible, only the reconstructions of the real part are shown. From the reconstructions, the two cylinders are clearly visible with their estimated relative permittivity values reaching a maximum $\approx$3.5. For all separations, a 'hole' artifact appears in the middle of each cylinder; this is not a deficiency in FEM-CSI as compared to IE-CSI but rather due to the quality of the data collected, and is demonstrated by running the same data with the IE-CSI algorithm. The IE-CSI result using the experimental dataset with $d = 0.01$ m separation is shown in figure 7.

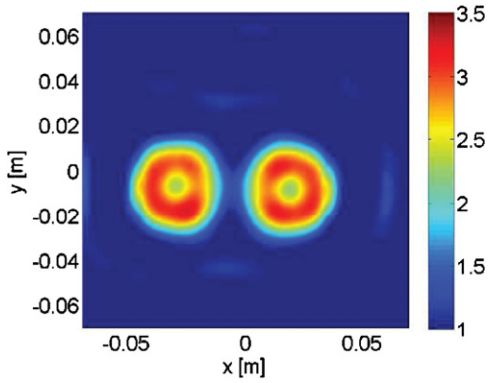

Figure 7. IE-CSI reconstructions at $f = 4.5$ GHz for experimental datasets of two nylon-66 rods separated by 0.01 m.

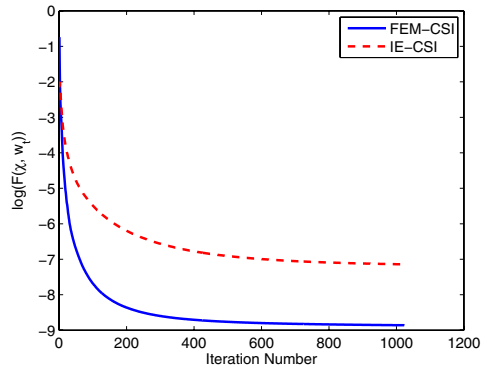

(a) Ü-profile

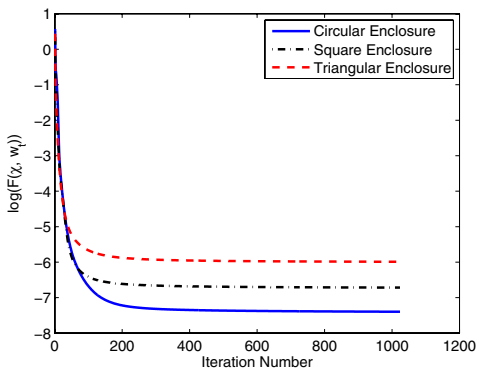

(b) MWT in PEC enclosures

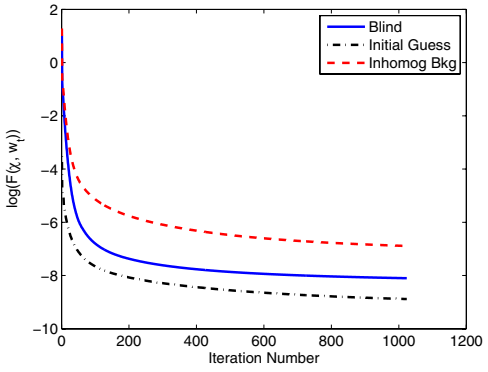

(c) BMI of brain model

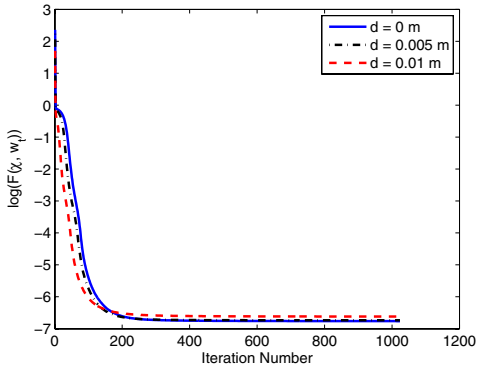

(d) Experiemental datasets

Figure 8. The FEM-CSI cost functional, $\mathcal{F}(\chi, w_t)$, versus the iteration number for (a) Ü-profile, (b) MWT in PEC enclosures, (c) BMI of the brain model and (d) experimental datasets reconstruction.

6. Conclusion

The full derivation of a new CSI algorithm incorporating the flexibility of the finite-element method to discretize the Helmholtz partial differential equation operator in the formulation of the electromagnetic inverse problem has been given. Results of applying this FEM-CSI algorithm to synthetic and experimental datasets have been presented and the advantages of the algorithm have been demonstrated by applying it to MWI setups using PEC enclosures of various shapes as well as using prior information in the form of an inhomogeneous background for the inverse problem. The ability to use adaptive non-uniform meshes with finer resolution in regions exhibiting large gradients in the dielectric contrast is also a possibility using this algorithm and is a topic for future study. The addition of multiplicative regularization is also a relatively straightforward improvement which will be dealt with in a future publication.

Acknowledgments

The authors acknowledge the financial support of NSERC, MITACS, CancerCare Manitoba and the University of Manitoba Graduate Fellowship. We also thank Dr Puyan Mojabi for fruitful discussions.

Appendix A. Derivation of the gradient used in the FEM-CSI algorithm

In the first step of the FEM-CSI algorithm, the gradient, g_t, of the cost functional with respect to the contrast source variables, w_t, is required to calculate the updates. At a given point w_t, g_t is a vector pointing in the direction in which the Gâteaux differential has the largest value.

The Gâteaux differential is evaluated first for the data misfit function $\mathcal{F}^{\mathcal{S}}(w_t)$ and then for the domain equation $\mathcal{F}^{\mathcal{D}}(\chi, w_t)$. For a small variation in w_t taken along the search direction h_t, the Gâteaux differential of the data misfit function $\mathcal{F}^{\mathcal{S}}(w_t)$ is given by

$$\begin{aligned}
d_{h_t}\mathcal{F}^{\mathcal{S}}(w_t) &= \lim_{\epsilon\to 0} \frac{\mathcal{F}^{\mathcal{S}}(w_t+\epsilon h_t) - \mathcal{F}^{\mathcal{S}}(w_t)}{\epsilon} \\
&= \lim_{\epsilon\to 0} \eta^{\mathcal{S}} \frac{\|f_t - \boldsymbol{\mathcal{M}}_{\mathcal{S}}\boldsymbol{\mathcal{L}}[w_t+\epsilon h_t]\|_{\mathcal{S}}^2 - \|\rho_t\|_{\mathcal{S}}^2}{\epsilon} \\
&= \lim_{\epsilon\to 0} \eta^{\mathcal{S}} \frac{\|\rho_t - \epsilon\boldsymbol{\mathcal{M}}_{\mathcal{S}}\boldsymbol{\mathcal{L}}[h_t]\|_{\mathcal{S}}^2 - \|\rho_t\|_{\mathcal{S}}^2}{\epsilon} \\
&= \lim_{\epsilon\to 0} \eta^{\mathcal{S}} \frac{\|\rho_t\|_{\mathcal{S}}^2 - 2\epsilon\mathrm{Re}\,\langle\boldsymbol{\mathcal{M}}_{\mathcal{S}}\boldsymbol{\mathcal{L}}[h_t], \rho_t\rangle_{\mathcal{S}} + \epsilon^2\|\boldsymbol{\mathcal{M}}_{\mathcal{S}}\boldsymbol{\mathcal{L}}[h_t]\|_{\mathcal{S}}^2 - \|\rho_t\|_{\mathcal{S}}^2}{\epsilon} \\
&= \lim_{\epsilon\to 0} \eta^{\mathcal{S}} \frac{-2\epsilon\mathrm{Re}\,\langle\boldsymbol{\mathcal{M}}_{\mathcal{S}}\boldsymbol{\mathcal{L}}[h_t], \rho_t\rangle_{\mathcal{S}} + \epsilon^2\|\boldsymbol{\mathcal{M}}_{\mathcal{S}}\boldsymbol{\mathcal{L}}[h_t]\|_{\mathcal{S}}^2}{\epsilon} \\
&= \mathrm{Re}\langle -2\eta^{\mathcal{S}}\boldsymbol{\mathcal{M}}_{\mathcal{S}}\boldsymbol{\mathcal{L}}[h_t], \rho_t\rangle_{\mathcal{S}}. \qquad \text{(A.1)}
\end{aligned}$$

Here ρ_t is a function of w_t, given as

$$\rho_t = f_t - \boldsymbol{\mathcal{M}}_{\mathcal{S}}\boldsymbol{\mathcal{L}}[w_t]. \qquad \text{(A.2)}$$

Next, to obtain the direction h_t that will maximize the differential, the direction h_t can be isolated in the inner product using the adjoint operator $\boldsymbol{\mathcal{G}}^{\mathcal{S}}$ which satisfies

$$\langle -2\eta^{\mathcal{S}}\boldsymbol{\mathcal{M}}_{\mathcal{S}}\boldsymbol{\mathcal{L}}[h_t], \rho_t\rangle_{\mathcal{S}} = \langle h_t, \boldsymbol{\mathcal{G}}^{\mathcal{S}}[\rho_t]\rangle_{\mathcal{D}}. \qquad \text{(A.3)}$$

Using the inner product definitions given in (15) and (17), both sides of (A.3) are expanded as follows:

$$-2\eta^{\mathcal{S}}\rho_t^H\boldsymbol{\mathcal{M}}_{\mathcal{S}}\boldsymbol{\mathcal{L}}[h_t] = \rho_t^H(\boldsymbol{\mathcal{G}}^{\mathcal{S}})^H\mathbf{T}_{\mathcal{D}}h_t. \qquad \text{(A.4)}$$

It can be easily shown that $\mathcal{G}^{\mathcal{S}} = -2\eta^{\mathcal{S}}\mathbf{T}_{\mathcal{D}}^{-1}\mathcal{L}^H\mathcal{M}_{\mathcal{S}}^H$, and the Gâteaux differential can thus be written as

$$d_{h_t}\mathcal{F}^{\mathcal{S}}(w_t) = \mathrm{Re}\langle h_t, -2\eta^{\mathcal{S}}\mathbf{T}_{\mathcal{D}}^{-1}\mathcal{L}^H\mathcal{M}_{\mathcal{S}}^H\rho_t\rangle_{\mathcal{D}}. \tag{A.5}$$

To maximize the value of the differential, the search direction h_t is chosen as

$$h_t = -2\eta^{\mathcal{S}}\mathbf{T}_{\mathcal{D}}^{-1}\mathcal{L}^H\mathcal{M}_{\mathcal{S}}^H\rho_t. \tag{A.6}$$

This search direction h_t is the gradient of the data misfit $\mathcal{F}^{\mathcal{S}}(w_t)$ with respect to the contrast source variables w_t.

Next the Gâteaux differential of the domain equation $\mathcal{F}^{\mathcal{D}}(\chi, w_t)$ is evaluated, with the contrast, χ, held constant. For a small variation in w_t taken along the search direction h_t, the Gâteaux differential of $\mathcal{F}^{\mathcal{D}}(\chi, w_t)$ is given by

$$\begin{aligned} d_{h_t}\mathcal{F}^{\mathcal{D}}(\chi, w_t) &= \lim_{\epsilon\to 0}\frac{\mathcal{F}^{\mathcal{D}}(\chi, w_t+\epsilon h_t) - \mathcal{F}^{\mathcal{D}}(\chi, w_t)}{\epsilon} \\ &= \lim_{\epsilon\to 0}\eta^{\mathcal{D}}\frac{\|r_t - \epsilon(h_t - \chi\odot\mathcal{M}_{\mathcal{D}}\mathcal{L}[h_t])\|_{\mathcal{D}}^2 - \|r_t\|_{\mathcal{D}}^2}{\epsilon} \\ &= \lim_{\epsilon\to 0}\eta^{\mathcal{D}}\frac{-2\epsilon\mathrm{Re}\,\langle(h_t - \chi\odot\mathcal{M}_{\mathcal{D}}\mathcal{L}[h_t]), r_t\rangle_{\mathcal{D}} + \epsilon^2\|h_t - \chi\odot\mathcal{M}_{\mathcal{D}}\mathcal{L}[h_t]\|_{\mathcal{D}}^2}{\epsilon} \\ &= \mathrm{Re}\langle -2\eta^{\mathcal{D}}(h_t - \chi\odot\mathcal{M}_{\mathcal{D}}\mathcal{L}[h_t]), r_t\rangle_{\mathcal{D}}. \end{aligned} \tag{A.7}$$

Here r_t is taken to be a residual in the domain equation, which is a function of w_t and is given by

$$r_t = \chi\odot E_t^{\mathrm{inc}} - w_t + \chi\odot\mathcal{M}_{\mathcal{D}}\mathcal{L}[w_t]. \tag{A.8}$$

To evaluate the direction h_t that maximizes the differential, the differential is rewritten so as to isolate the direction h_t using an adjoint operator $\mathcal{G}^{\mathcal{D}}$ which satisfies

$$\langle -2\eta^{\mathcal{D}}(h_t - \chi\odot\mathcal{M}_{\mathcal{D}}\mathcal{L}[h_t]), r_t\rangle_{\mathcal{D}} = \langle h_t, \mathcal{G}^{\mathcal{D}}[r_t]\rangle_{\mathcal{D}}. \tag{A.9}$$

Utilizing (15), the expansion of the inner products results in

$$-2\eta^{\mathcal{D}}r_t^H\mathbf{T}_{\mathcal{D}}(\mathbf{I} - \mathbf{X}\mathcal{M}_{\mathcal{D}}\mathcal{L})h_t = r_t^H(\mathcal{G}^{\mathcal{D}})^H\mathbf{T}_{\mathcal{D}}h_t, \tag{A.10}$$

where $\mathbf{I}\in\mathbb{R}^{I\times I}$ is an identity matrix and $\mathbf{X} = \mathrm{diag}(\chi)$ is a diagonal matrix. Solving for $\mathcal{G}^{\mathcal{D}}$ we obtain

$$\mathcal{G}^{\mathcal{D}} = -2\eta^{\mathcal{D}}\mathbf{T}_{\mathcal{D}}^{-1}\big(\mathbf{I} - \mathcal{L}^H\mathcal{M}_{\mathcal{D}}^T\mathbf{X}^H\big)\mathbf{T}_{\mathcal{D}}. \tag{A.11}$$

The Gâteaux differential of the domain equation $\mathcal{F}^{\mathcal{D}}(\chi, w_t)$ becomes

$$d_{h_t}\mathcal{F}^{\mathcal{D}}(\chi, w_t) = \mathrm{Re}\big\langle h_t, -2\eta^{\mathcal{D}}\mathbf{T}_{\mathcal{D}}^{-1}\big(\mathbf{I} - \mathcal{L}^H\mathcal{M}_{\mathcal{D}}^T\mathbf{X}^H\big)\mathbf{T}_{\mathcal{D}}r_t\big\rangle_{\mathcal{D}}. \tag{A.12}$$

Thus, to maximize the Gâteaux differential, the search direction h_t is chosen as

$$h_t = -2\eta^{\mathcal{D}}\mathbf{T}_{\mathcal{D}}^{-1}\big(\mathbf{I} - \mathcal{L}^H\mathcal{M}_{\mathcal{D}}^T\mathbf{X}^H\big)\mathbf{T}_{\mathcal{D}}r_t. \tag{A.13}$$

This is the gradient of the domain equation $\mathcal{F}^{\mathcal{D}}(\chi, w_t)$ with respect to the contrast source variables w_t.

Furthermore at the nth iteration of the algorithm, the gradient of the cost functional for contrast source variables $w_{t,n-1}$ and contrast variables χ_{n-1} is

$$g_{t,n} = -2\eta^{\mathcal{S}}{\mathbf{T}_{\mathcal{D}}}^{-1}\mathcal{L}^H\mathcal{M}_{\mathcal{S}}^H\rho_{t,n-1} - 2\eta_n^{\mathcal{D}}\mathbf{T}_{\mathcal{D}}^{-1}\big(\mathbf{I} - \mathcal{L}^H\mathcal{M}_{\mathcal{D}}^T\mathbf{X}_{n-1}^H\big)\mathbf{T}_{\mathcal{D}}r_{t,n-1}. \tag{A.14}$$

Appendix B. Derivation of the contrast variables update

In the second step of the FEM-CSI method, a new contrast χ is chosen which minimizes the modified domain equation

$$\mathcal{F}_m^{\mathcal{D}}(\chi) = \sum_t \|\mathbf{E}_t\chi - w_t\|_{\mathcal{D}}^2, \tag{B.1}$$

where $\mathbf{E}_t \in \mathbb{C}^{I\times I}$ is the total field diagonal matrix with diagonal entities equal to the elements of vector $E_t = E_t^{\text{inc}} + \boldsymbol{\mathcal{M}}_{\mathcal{D}}\boldsymbol{\mathcal{L}}[w_t]$. In this step the contrast source w_t is kept constant.

The minimizer of $\mathcal{F}_m^{\mathcal{D}}(\chi)$ is obtained by first evaluating the Gâteaux differential. For a small variation with respect to χ along a search direction h, the differential is calculated as

$$\begin{aligned}
d_h\mathcal{F}_m^{\mathcal{D}}(\chi) &= \lim_{\epsilon\to 0}\frac{1}{\epsilon}\left[\sum_t \|\mathbf{E}_t(\chi+\epsilon h) - w_t\|_{\mathcal{D}}^2 - \sum_t \|\mathbf{E}_t\chi - w_t\|_{\mathcal{D}}^2\right]\\
&= \lim_{\epsilon\to 0}\frac{1}{\epsilon}\left[\sum_t \|(\mathbf{E}_t\chi - w_t) + \epsilon\mathbf{E}_t h)\|_{\mathcal{D}}^2 - \sum_t \|\mathbf{E}_t\chi - w_t\|_{\mathcal{D}}^2\right]\\
&= \lim_{\epsilon\to 0}\frac{1}{\epsilon}\left[\sum_t \|r_t + \epsilon\mathbf{E}_t h\|_{\mathcal{D}}^2 - \sum_t \|r_t\|_{\mathcal{D}}^2\right]\\
&= \lim_{\epsilon\to 0}\frac{1}{\epsilon}\left[\sum_t \|r_t\|_{\mathcal{D}}^2 + 2\epsilon\sum_t \operatorname{Re}\langle r_t, \mathbf{E}_t h\rangle_{\mathcal{D}} + \epsilon^2\sum_t \|\mathbf{E}_t h\|_{\mathcal{D}}^2 - \sum_t \|r_t\|_{\mathcal{D}}^2\right]\\
&= 2\sum_t \operatorname{Re}\langle r_t, \mathbf{E}_t h\rangle_{\mathcal{D}}\\
&= 2\sum_t \operatorname{Re}\left(h^H\mathbf{E}_t^H\mathbf{T}_{\mathcal{D}}r_t\right)\\
&= 2\operatorname{Re}\left\langle\sum_t \mathbf{E}_t^H\mathbf{T}_{\mathcal{D}}r_t, h\right\rangle.
\end{aligned} \tag{B.2}$$

Here $r_t = \mathbf{E}_t\chi - w_t$, and for any arbitrary vectors a and b the inner product $\langle a, b\rangle = b^H a$. Next, the search direction that will maximize the Gâteaux differential is $h = \sum_t \mathbf{E}_t^H\mathbf{T}_{\mathcal{D}}r_t$. Thus, at the nth iteration the gradient of the modified domain equation with respect to the contrast variable χ_n is

$$\nabla\mathcal{F}_m^{\mathcal{D}}(\chi)\big|_{\chi=\chi_n} = \sum_t \mathbf{E}_{t,n}^H\mathbf{T}_{\mathcal{D}}(\mathbf{E}_{t,n}\chi_n - w_{t,n}). \tag{B.3}$$

The χ_n that minimizes $\mathcal{F}_m^{\mathcal{D}}(\chi_n)$ is found by setting (B.3) to zero, requiring the solution of

$$\left(\sum_t \mathbf{E}_{t,n}^H\mathbf{T}_{\mathcal{D}}\mathbf{E}_{t,n}\right)\chi_n = \sum_t \mathbf{E}_{t,n}^H\mathbf{T}_{\mathcal{D}}w_{t,n}. \tag{B.4}$$

Since $\mathbf{E}_{t,n}$ is a diagonal matrix and $\mathbf{T}_{\mathcal{D}}$ is sparse, the minimizer χ_n can be calculated efficiently.

Appendix C. Derivation of the initial guess for FEM-CSI

An initial guess to begin the FEM-CSI updating procedure is found by calculating the contrast sources which minimize $\mathcal{F}^{\mathcal{S}}(w_t)$ in the steepest-descent direction, starting with a zero initial guess. Note that this is the standard starting technique when applying most variations of the conjugate-gradient technique. For a single transmitter, the data misfit $\mathcal{F}_t^{\mathcal{S}}(w_t)$ is

$$\mathcal{F}_t^{\mathcal{S}}(w_t) = \|f_t - \boldsymbol{\mathcal{M}}_{\mathcal{S}}\boldsymbol{\mathcal{L}}[w_t]\|_{\mathcal{S}}^2. \tag{C.1}$$

As derived in appendix A, at the nth iteration, the gradient of $\mathcal{F}_t^{\mathcal{S}}(w_t)$ with respect to the contrast source variable $w_{t,n-1}$ is given by

$$\nabla \mathcal{F}_t^{\mathcal{S}}(w_t)\big|_{w_t=w_{t,n-1}} = -2\eta^{\mathcal{S}} \mathbf{T}_{\mathcal{D}}^{-1} \mathcal{L}^H \mathcal{M}_{\mathcal{S}}^H \rho_{t,n-1} = \mathcal{G}^{\mathcal{S}} \rho_{t,n-1}, \tag{C.2}$$

where $\rho_{t,n-1} = f_t - \mathcal{M}_{\mathcal{S}} \mathcal{L}[w_{t,n-1}]$.

The update equation for the first iteration of the method of steepest descent is

$$w_{t,0} = w_{t,-1} - \beta_0 \mathcal{G}^{\mathcal{S}} \rho_{t,-1}, \tag{C.3}$$

where $w_{t,-1}$ is the initial guess for the method of steepest descent which will be set to zero, and β_0 is a real update coefficient selected to minimize $\mathcal{F}_t^{\mathcal{S}}(w_{t,-1} - \beta_0 \mathcal{G}^{\mathcal{S}} \rho_{t,-1})$.

Once β_0 is found, $w_{t,0}$ becomes the initial guess for the FEM-CSI updating procedure. Thus, we have

$$w_{t,0} = -\beta_0 \mathcal{G}^{\mathcal{S}} f_t. \tag{C.4}$$

To find β_0, (C.4) is substituted into $\mathcal{F}_t^{\mathcal{S}}(w_t)$ giving

$$\begin{aligned}\mathcal{F}_t^{\mathcal{S}}(w_{t,0}) &= \| f_t + \beta_0 \mathcal{M}_{\mathcal{S}} \mathcal{L}[\mathcal{G}^{\mathcal{S}} f_t] \|_{\mathcal{S}}^2 \\ &= (f_t + \beta_0 \mathcal{M}_{\mathcal{S}} \mathcal{L}[\mathcal{G}^{\mathcal{S}} f_t])^H (f_t + \beta_0 \mathcal{M}_{\mathcal{S}} \mathcal{L}[\mathcal{G}^{\mathcal{S}} f_t]) \\ &= \| f_t \|_{\mathcal{S}}^2 + 2\beta_0 \mathrm{Re}\langle \mathcal{M}_{\mathcal{S}} \mathcal{L}[\mathcal{G}^{\mathcal{S}} f_t],\, f_t \rangle_{\mathcal{S}} + \beta_0^2 \| \mathcal{M}_{\mathcal{S}} \mathcal{L}[\mathcal{G}^{\mathcal{S}} f_t] \|_{\mathcal{S}}^2. \end{aligned} \tag{C.5}$$

Differentiating with respect to the real scalar variable β_0 gives

$$\frac{\partial \mathcal{F}_t^{\mathcal{S}}}{\partial \beta_0} = 2\,\mathrm{Re}\langle \mathcal{M}_{\mathcal{S}} \mathcal{L}[\mathcal{G}^{\mathcal{S}} f_t],\, f_t \rangle_{\mathcal{S}} + 2\beta_0 \| \mathcal{M}_{\mathcal{S}} \mathcal{L}[\mathcal{G}^{\mathcal{S}} f_t] \|_{\mathcal{S}}^2, \tag{C.6}$$

which is set equal to zero to give the following formula for β_0:

$$\beta_0 = -\frac{\mathrm{Re}\langle \mathcal{M}_{\mathcal{S}} \mathcal{L}[\mathcal{G}^{\mathcal{S}} f_t],\, f_t \rangle_{\mathcal{S}}}{\| \mathcal{M}_{\mathcal{S}} \mathcal{L}[\mathcal{G}^{\mathcal{S}} f_t] \|_{\mathcal{S}}^2}. \tag{C.7}$$

Substituting (C.7) into (C.4), the initial guess for the FEM-CSI updating procedure becomes

$$w_{t,0} = \frac{\mathrm{Re}\langle \mathcal{M}_{\mathcal{S}} \mathcal{L}[\mathcal{G}^{\mathcal{S}} f_t],\, f_t \rangle_{\mathcal{S}}}{\| \mathcal{M}_{\mathcal{S}} \mathcal{L}[\mathcal{G}^{\mathcal{S}} f_t] \|_{\mathcal{S}}^2} \mathcal{G}^{\mathcal{S}} f_t. \tag{C.8}$$

References

[1] Abubakar A, Habashy T M, Druskin V, Knizhnerman L and Alumbaugh D L 2008 Two-and-half dimensional forward and inverse modelling for the interpretation of low-frequency electromagnetic measurements *Geophysics* **73** F165–77

[2] Meaney P M, Fanning M W, Li D, Poplack S P and Paulsen K D 2000 A clinical prototype for active microwave imaging of the breast *IEEE Trans. Microw. Theory Tech.* **48** 1841–53

[3] Bulyshev A E, Souvorov A E, Semenov S Y, Posukh V G and Sizov Y E 2004 Three dimensional vector microwave tomography: theory and computational experiments *Inverse Problems* **20** 1239–59

[4] Habashy T M and Abubakar A 2004 A general framework for constraint minimization for the inversion of electromagnetic measurements *Prog. Electromagn. Res.* **46** 265–312

[5] Mojabi P and LoVetri J 2009 Overview and classification of some regularization techniques for the Gauss–Newton inversion method applied to inverse scattering problems *IEEE Antennas Wirel. Propag. Lett.* **8** 645–8

[6] Caorsi S, Massa A, Pastorino M, Raffetto M and Randazzo A 2003 Detection of buried inhomogeneous elliptic cylinders by a memetic algorithm *IEEE Trans. Antennas Propag.* **51** 2878–84

[7] Caorsi S, Massa A, Pastorino M and Rosani A 2004 Microwave medical imaging: potentialities and limitations of a stochastic optimization technique *IEEE Trans. Microw. Theory Tech.* **52** 1909–16

[8] Donelli M, Franceschini G, Martini A and Massa A 2006 An integrated multiscaling strategy based on a particle swarm algorithm for inverse scattering problems *IEEE Trans. Geosci. Remote Sens.* **44** 298–312

[9] Rocca P, Benedetti M, Donelli M, Franceschini D and Massa A 2009 Evolutionary optimization as applied to inverse scattering problems *Inverse Problems* **25** 123003

[10] Gilmore C and LoVetri J 2008 Enhancement of microwave tomography through the use of electrically conducting enclosures *Inverse Problems* **24** 035008

[11] Lencrerot R, Litman A, Tortel H and Geffrin J-M 2009 Measurement strategies for a confined microwave circular scanner *Inverse Problems Sci. Eng.* **17** 787–802
[12] Mojabi P, Gilmore C, Zakaria A and LoVetri J 2009 Biomedical microwave inversion in conducting cylinders of arbitrary shapes *13th Int. Symp. Antenna Technology and Applied Electromagnetics and the Canadian Radio Science Meeting (ANTEM/URSI)* pp 1–4
[13] Mojabi P and LoVetri J 2010 Eigenfunction contrast source inversion for circular metallic enclosures *Inverse Problems* **26** 025010
[14] Chew W C and Wang Y M 1990 Reconstruction of two-dimensional permittivity distribution using the distorted born iterative method *IEEE Trans. Med. Imaging* **9** 218–25
[15] Mojabi P and LoVetri J 2009 Microwave biomedical imaging using the multiplicative regularized gauss-newton inversion *IEEE Antennas Wirel. Propag. Lett.* **8** 645–8
[16] Rekanos I T, Yioultsis T V and Tsiboukis T D 1999 Inverse scattering using the finite-element method and a nonlinear optimization technique *IEEE Trans. Microw. Theory Tech.* **47** 36–344
[17] Abubakar A, Hu W, van den Berg P M and Habashy T M 2008 A finite-difference contrast source inversion method *Inverse Problems* **24** 065004
[18] Paulsen K D, Meaney P M, Moskowitz M J, Sullivan J and Sullivan J M Jr 1995 A dual mesh scheme for finite element based reconstruction algorithms *IEEE Trans. Med. Imaging* **14** 504–14
[19] van den Berg P M and Kleinman R E 1997 A contrast source inversion method *Inverse Problems* **13** 1607–20
[20] van den Berg P M, van Broekhoven A L and Abubakar A 1999 Extended contrast source inversion *Inverse Problems* **15** 1325–44
[21] Abubakar A, van den Berg P M and Mallorqui J J 2002 Imaging of biomedical data using a multiplicative regularized contrast source inversion method *IEEE Trans. Microw. Theory Tech.* **50** 1761–77
[22] Abubakar A, van den Berg P M and Habashy T M 2005 Application of the multiplicative regularized contrast source inversion method on TM- and TE-polarized experimental Fresnel data *Inverse Problems* **21** S5–13
[23] Abubakar A, van den Berg P M and Semenov S Y 2003 Two- and three-dimensional algorithms for microwave imaging and inverse scattering *J. Electromagn. Waves Appl.* **17** 209–31
[24] Gilmore C, Abubakar A, Hu W, Habashy T M and van den Berg P M 2009 Microwave biomedical data inversion using the finite-difference contrast source inversion method *IEEE Trans. Antennas Propag.* **57** 1528–38
[25] Zakaria A, Gilmore C and LoVetri J 2010 A finite-element contrast source inversion method for microwave tomography *26th Int. Rev. Progress in ACES Conf.*
[26] Gilmore C, Mojabi P, Zakaria A, Ostadrahimi M, Kaye C, Noghanian S, Shafai L, Pistorius S and LoVetri J 2010 A wideband microwave tomography system with a novel frequency selection procedure *IEEE Trans. Biomed. Eng.* **57** 894–904
[27] Meaney P M, Fanning M W, Raynolds T, Fox C J, Fang Q, Kogel C A, Poplack S P and Paulsen K D 2007 Initial clinical experience with microwave breast imaging in women with normal mammography *Acad. Radiol.* **14** 207–18
[28] Jin J 2002 *The Finite Element Method in Electromagnetics* (New York: Wiley)
[29] Davis T A and Duff I S 1997 An unsymmetric-pattern multifrontal method for sparse LU factorization *Siam J. Matrix Anal. Appl.* **18** 140–58
[30] Davis T A 2004 A column pre-ordering strategy for unsymmetric-pattern multifrontal method *ACM Trans. Math. Softw.* **30** 165–95
[31] Schenk O and Gärtner K 2009 Parallel sparse direct and multi-recursive iterative linear solvers (PARDISO) user guide version 4.0.0
[32] Geuzaine C and Remacle J-F 2009 Gmsh: a 3-D finite element mesh generator with built-in pre- and post-processing facilities *Int. J. Numer. Methods Eng.* **79** 1309–31
[33] Meaney P M, Demidenko E, Yagnamurthy N K, Li D, Fanning M W and Paulsen K D 2001 A two-stage microwave image reconstruction procedure for improved internal feature extraction *Med. Phys.* **28** 2358–69
[34] Abubakar A, van den Berg P M and Semenov S Y 2004 A robust iterative method for Born inversion *IEEE Trans. Geosci. Remote Sens.* **42** 342–54
[35] Semenov S Y and Corfield D R 2008 Microwave tomography for brain imaging: feasibility assessment for stroke detection *Int. J. Antennas Propag.* **2008** 254830
[36] Gabriel C, Gabriel S and Corthout E 2000 The dielectric properties of biological tissues: III. Parametric models for the dielectric spectrum of tissues *Phys. Med. Biol.* **41** 2271–94
[37] Gilmore C, Mojabi P, Zakaria A, Ostadrahimi M, Kaye C, Noghanian S, Shafai L, Pistorius S and LoVetri J 2009 An ultra-wideband microwave tomography system: preliminary results *Engineering in Medicine and Biology Society, EMBC 2009. Annu. Int. Conf. IEEE* pp 2288–91
[38] Gilmore C, Mojabi P, Zakaria A, Pistorius S and LoVetri J 2010 On super-resolution with an experimental microwave tomography system *IEEE Antennas Wirel. Propag. Lett.* **9** 393–6